



Direct current (DC) resistivity and induced polarization (IP) monitoring of active layer dynamics at high temporal resolution



Joseph Doetsch^{a,b,*}, Thomas Ingeman-Nielsen^c, Anders V. Christiansen^b, Gianluca Fiandaca^b, Esben Auken^b, Bo Elberling^d

^a SCCER-SoE, ETH Zurich, Zurich, Switzerland

^b Department of Geoscience, Aarhus University, Aarhus, Denmark

^c Department of Civil Engineering, Technical University of Denmark, Lyngby, Denmark

^d Center for Permafrost (CENPERM), Department of Geosciences and Natural Resource Management, University of Copenhagen, Øster Voldgade 10, DK-1350 Copenhagen K., Denmark

ARTICLE INFO

Article history:

Received 18 September 2014

Received in revised form 24 June 2015

Accepted 3 July 2015

Available online 11 July 2015

Keywords:

Active layer

Electrical resistivity

Induced polarization

Monitoring

Greenland

Permafrost

ABSTRACT

With permafrost thawing and changes in active layer dynamics induced by climate change, interactions between biogeochemical and thermal processes in the ground are of great importance. Here, active layer dynamics have been monitored using direct current (DC) resistivity and induced polarization (IP) measurements at high temporal resolution and at a relatively large scale at a heath tundra site on Disko Island on the west coast of Greenland (69°N). At the field site, the active layer is disconnected from the deeper permafrost, due to isothermal springs in the region. Borehole sediment characteristics and subsurface temperatures supplemented the DC-IP measurements. A time-lapse DC-IP monitoring system has been acquiring at least six datasets per day on a 42-electrode profile with 0.5 m electrode spacing since July 2013. Remote control of the data acquisition system enables interactive adaptation of the measurement schedule, which is critically important to acquire data in the winter months, where extremely high contact resistances increase the demands on the resistivity meter. Data acquired during the freezing period of October 2013 to February 2014 clearly image the soil freezing as a strong increase in resistivity. While the freezing horizon generally moves deeper with time, some variations in the freezing depth are observed along the profile. Comparison with depth-specific soil temperature indicates an exponential relationship between resistivity and below-freezing temperature. Time-lapse inversions of the full-decay IP data indicate a decrease of normalized chargeability with freezing of the ground, which is the result of a decrease in the total unfrozen water and of the higher ion concentration in the pore-water. We conclude that DC-IP time-lapse measurements can non-intrusively and reliably image freezing patterns and their lateral variation on a 10–100 m scale that is difficult to sample by point measurements. In combination with laboratory experiments, the different patterns in resistivity and chargeability changes will enable the disentanglement of processes (e.g., fluid migration and freezing, advective and diffusive heat transport) occurring during freezing of the ground. The technology can be expanded to three dimensions and also to larger scale.

© 2015 Elsevier B.V. All rights reserved.

1. Introduction

Twenty-five percent of the Earth's land area is underlain by permafrost, which has been frozen for at least two consecutive years (Anisimov and Nelson, 1996). The active layer covering the permafrost thaws every year and has increased in thickness over large tracts of the Arctic (Mishra and Riley, 2014) due to climate change. Cold temperatures and long cold-seasons in the Arctic keep nutrient availabilities and thereby primary production low. However, there is an increasing interest in the active layer processes as easily available forms of carbon and nitrogen are being released upon stimulated microbial decomposition of soil organic matter in the Arctic (Wild et al., 2014). This will play

a critical role for the release of greenhouse gases (Hayes et al., 2014), and it will affect the timing of nutrient availability for plants upon springtime when the active layer thaws from above. In this way the active layer dynamics control both the potential carbon release measured as decomposition of organic matter, but also the C sink strength of the Arctic biosphere measured as increasing nutrient availability and plant growth (Hollesen et al., 2011).

Freeze–thaw dynamics within the active layer and top permafrost are closely linked to the availability of water and salt in the ground, which influence the freezing point depression and ions (nutrient) translocation in the profile. However, despite the importance of high-resolution data on active layer and top permafrost dynamics, data are limited due to difficulties associated with repeated non-destructive sampling of the active layer under in-situ conditions during the critical time periods of freezing and thawing. Temperature and other depth-

* Corresponding author at: ETH Zurich, Sonneggstr. 5, NO F27, 8092 Zurich, Switzerland.
E-mail address: joseph.doetsch@erdw.ethz.ch (J. Doetsch).

resolved information such as soil moisture are typically restricted to few point locations and are hard to extend to a larger scale.

Geophysical measurements can image permafrost and the active layer at a larger scale of tens to hundreds of meters. For example, Hubbard et al. (2013a) combine LiDAR and geophysical datasets in a cluster analysis to detect zones with different geomorphic, hydrological, thermal and geochemical properties. Gangodagamage et al. (2014) calibrate satellite data with ground truth and are able to predict both small and larger scale variations in active layer thickness across an area of 300×500 m. Electrical properties of the shallow subsurface at the scale of a few hundred meters can be sensed by electromagnetic induction data, and Dafflon et al. (2013) have shown their potential for active layer mapping.

While these LiDAR, satellite and electromagnetic induction data are able to cover large areas, they are not suited for continuous monitoring of active layer dynamics, because they cannot provide continuous measurement time-series. Methods that use permanent installations such as electrical resistance tomography with buried electrodes are better suited for this purpose, and they yield a relatively high spatial and temporal resolution. Time-lapse inversion of repeated direct current (DC) measurements allows both active layer dynamics and interannual permafrost conditions to be delineated vertically as well as laterally, where especially the lateral variations are difficult to obtain from drillings alone. Hauck (2002) introduced DC resistivity for monitoring of alpine permafrost and showed that variations in electrical resistivity can be used to determine the freezing depth. Analyses of a comprehensive DC resistivity monitoring dataset from a 7-year study at Schilthorn, Swiss Alps (Hilbich et al., 2008, 2011) have proven the applicability of DC for monitoring of freezing and thawing processes on short-term, seasonal, and long-term scales. The DC resistivity monitoring examples of alpine permafrost also include hard rock targets (Krautblatter and Hauck, 2007; Krautblatter et al., 2010), which require special electrode design and instrument settings, such as using high voltages, because even the thawed rocks have resistivities larger than $10 \text{ k}\Omega\text{m}$ and current injection is very difficult. To our knowledge, in contrast to high altitude permafrost, no example of DC resistivity monitoring examples exists of Arctic permafrost.

The electrical resistivity of sediments and rocks is a function of porosity, water content, pore-water ion concentration, temperature and surface conductivity. Freezing of the rocks increases the electrical resistivity by transforming the electrical conductor water into the insulator ice. In unconsolidated sediments, there is typically an exponential increase of resistivity below 0°C temperature (Hoekstra et al., 1975), while a linear relationship has been reported for hard rock (Krautblatter et al., 2010). However, due to the other factors influencing resistivity, the inverted resistivity cannot be transformed directly into temperature, especially when changes in water saturation might happen simultaneously to freezing.

Measurements of induced polarization (IP) are sensitive to the grain surface to pore volume ratio and the grain surface charge (e.g., Lesmes and Frye, 2001; Slater and Lesmes, 2002) and can therefore help to image the different processes associated with freezing of sediments. IP monitoring has been used in field studies to image changes in geochemistry associated with bio-stimulation (Flores Orozco et al., 2011; Johnson et al., 2010; Williams et al., 2009) and CO_2 injection (Doetsch et al., 2015) in shallow aquifers, but no field study related to permafrost is known to us.

Wu et al. (2013) conducted laboratory column experiments to explore the potential of the frequency-domain complex resistivity method for monitoring the freeze-thaw transitions of the Arctic permafrost soils. Over two orders of magnitude of resistivity variations were observed when the temperature was increased or decreased between -20 and 0°C , and smaller resistivity variations were also observed during the isothermal thawing or freezing processes that occurred near 0°C . The IP phase response was found to be related to the unfrozen water in the soil matrix, and a shift of the observed spectral response to

lower frequency was observed during the isothermal thawing process, indicating a sequential thawing of fine particles within the soil matrix first and coarse particles thawing at later times. Laboratory measurements of Kemna et al. (2014) also indicate that some of the polarization mechanisms break down upon ice crystallization, decreasing the IP effect, in accordance with results of Wu et al. (2013).

The aim of this study is to demonstrate the use of DC and IP monitoring to quantify thaw-freeze dynamics at a High Arctic site in Greenland. We hypothesize that combined DC-IP measurements are able to capture hourly to daily variations in the electrical resistivity and thereby improve future assessment of temporal and spatial changes in water content and pore-water ion concentrations associated with freeze-thaw cycles in nature. For this purpose, we perform time-lapse DC and IP measurements of the ground during freezing in fall and winter (2013–2014) and test how combined DC-IP measurements improve the understanding of the processes occurring during freezing of the ground. To our knowledge this is the first reported field study of IP active-layer monitoring and the first DC monitoring study of Arctic permafrost and active layer at a relatively large spatial scale.

2. Field site

2.1. Field site characterization

The study site ($\text{N}69^\circ15'$, $\text{W}53^\circ30'$, 30 m a.s.l.) is an *Empetrum nigrum* and *Betula nana* heath tundra near the Arctic Station on Qeqertarsuaq/Disko Island on the west coast of Greenland (Fig. 1b). The island is

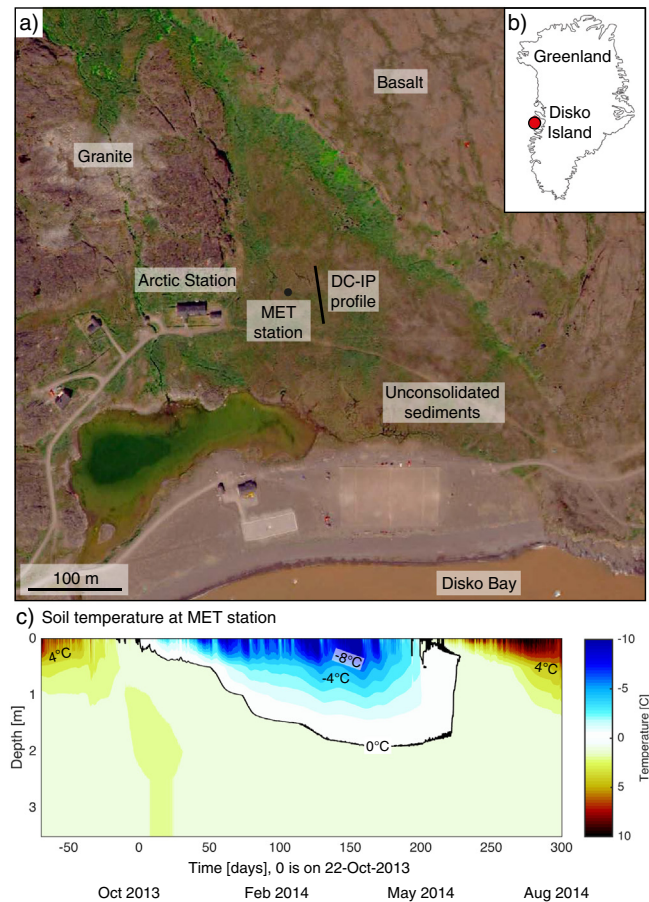


Fig. 1. General site information with an aerial photo of the field site on Disko Island in (a), its location in western Greenland in (b) and soil temperatures in (c). The DC-IP profile is installed on unconsolidated sediments at ~ 33 m elevation and the soil temperatures measured at the weather station (c) show temperature variation to a depth of approximately 2 m.

located near the transitional zone between the low and the high Arctic. According to the meteorological measurements of the station (1991–2004; Hansen et al., 2006) the mean air temperatures of the warmest (July) and the coldest (February–March) months are 7.1 and -16.0 °C. The mean annual soil temperature at 5 cm depth is -1.9 °C and the soil is frozen from October to late May. Below-freezing conditions typically prevail in the entire active soil layer from late December until May. Most years, a complete snow cover appears in October and approaches its maximum thickness by the end of the year. Pre-Quaternary formations found in the area include a crystalline basement (granite)—older than 1800 ma and Tertiary breccia and extensive plateau-basalt lavas (see indications on Fig. 1a). In some areas the formations are covered by Quaternary deposits including tills, marine interglacial sediments as well as Holocene lacustrine deposits. Our study area is situated in such an area, where the bedrock-valley was filled with loose sediments with an unusually high iron content due to the basaltic source rocks. While permafrost (to a depth >100 m) exists on Qeqertarsuaq, and permafrost features are numerous in the field area, shallow permafrost is not observed locally at the field installation. Measurements down to 3.5 m depth show that temperatures between 2 and 3.5 m depth are between 0 °C and 1 °C year-round (Fig. 1c). These relatively warm subsurface temperatures are due to water flow in the loose sediments that is fed by isothermal springs located North (uphill) of our field site. Due to the continuously running water from the thermal springs the shallow active layer and the deeper permafrost are disconnected. A weak soil development has resulted in a typically less than 1 m thick soil profile consisting of slightly acidic gravel soil with less than 5 cm topsoil (A-horizon) on top.

2.2. Weather station and boreholes

Weather data, including above- and below-ground temperatures, precipitation and soil moisture are continuously recorded at a full water and energy meteorological (MET) station about 100 m from Arctic Station. The MET station is connected to power and internet from the Arctic Station and data are continuously uploaded to an online database. Based on the availability of these key data series together with power and internet requirements, the DC-IP profile was placed 30 m east of the MET station (see Fig. 1a).

Borehole drilling was performed to determine the strata within the active layer and to install thermistors for measurements of subsurface temperatures. Two boreholes were drilled for this study using motorized hand-drilling equipment consisting of a Stihl drilling engine, an expandable drill string, and a 40-cm-long core barrel with a drill head. The drilling was performed in July so that the upper part was sampled unfrozen, the lower part frozen. The sediments recovered were classified in the field and represent an organic poor ($<1\%$ C) very coarse material consisting of alternating layers of sand gravel and stones. The ice content was low, but some ice features were observed. No cryoturbation or buried organic layers were noted. The root depth was roughly 40 cm.

One of the thermistor-equipped boreholes is located at the weather station, with thermistors between 10 and 350 cm depth. Each of the 10 thermistors in a borehole are individually calibrated and reach an accuracy of ± 0.1 °C. Temperatures are recorded every 30 min using a Campbell data logger. The soil temperature development at the installation from August 2013 until August 2014 is shown in Fig. 1c. A second borehole is located at the center of the DC-IP profile, with 15 thermistors at 10 cm vertical intervals from the surface to 1.4 m depth.

2.3. DC-IP acquisition system

The DC-IP profile was installed 30 m east of the MET station in north–south direction (Fig. 1a). The profile is located on unconsolidated sediments consisting of poorly sorted gravel with a wide grain size distribution. Several rocks of 10–50 cm diameter are also found within the

sediments. The DC-IP installation consists of 64 electrodes installed in a transect with an inline electrode spacing of 0.5 m for the 42 electrodes in the center and 2 m towards the ends of the line (Fig. 2a). The total profile length is 64 m, with a 20 m long high-resolution part in the center. The short electrode spacing in the center was chosen to maximize the shallow resolution in the center of the profile and the long offset towards the line ends was added to increase the depth penetration.

Stainless steel plate electrodes (dimensions of $10 \times 10 \times 0.6$ cm) with a surface area of 224 cm^2 are used to maximize electrode contact area. Ingeman-Nielsen et al. (2013) found that the contact resistances and DC monitoring data quality are much improved by using buried plate electrodes instead of conventional pin-electrodes. Following these results the electrodes were installed vertically and perpendicular to the profile direction, a few centimeters below the surface, to ensure a good coupling and to minimize contact resistances.

The 64 electrodes are connected to an ABEM Terrameter LS® resistivity meter in combination with an ABEM ES10-64 extension switchbox using multi-core cables so that any electrode can be addressed at any time. The resistivity meter is located next to the DC-IP profile and has wired internet and power access. Fig. 2b illustrates the setup of the resistivity meter with remote access and automatic backup. A local area network controlled through a router ensures fast and reliable communication between a network attached storage (NAS), a mini PC and the resistivity meter. The resistivity meter automatically copies all acquired data to the NAS, where they are mirrored to a second disk and permanently stored, before deleting data on the resistivity meter. The most important data (about 1.5% of the raw data amount) are uploaded to an online database at Aarhus University using a cloud solution at the NAS and the internet connection at the MET station. This internet access also allows remote access to the mini PC, which can then be used to manipulate the resistivity meter. The embedded linux system of the resistivity meter allows full control of the acquisition parameters so that the measurement sequence and timing of the measurements can be adapted remotely.

2.4. DC-IP data acquisition

The DC-IP monitoring system commenced data acquisition from July 17, 2013 until February 15, 2014 and included dipole–dipole and gradient-type configurations both within the central 0.5 m-electrode-spacing parts and the long profiles. Dipole–dipole configurations were chosen due to their high sensitivity to lateral changes and gradient-type configurations contribute very robust measurements with good depth penetration. Both configuration types were optimized to take advantage of the multi-channel capability of the resistivity meter. The full sequence was acquired every 8 h, so that three complete datasets are available per day. In order to test for diurnal variations, gradient-type configurations on the 0.5 m spaced section were acquired 12 times per day.

The system operated smoothly, acquiring 7359 data points per day. Each stacked measurement consists of a direct-current electrical resistance and 10 gates with induced-polarization decay measurements. Contact resistances were initially around 2 k Ω and allowed high-quality measurements. When ground temperatures started to fall below the freezing point at the end of October (Fig. 3a), electrode contact resistances began to increase (Fig. 3b) so that high voltages were needed to inject even small currents, increasing demands on the acquisition system. Measurements involving long electrode separations having an inherently weaker signal started to be problematic and were removed from the automatic acquisition on Nov. 26, 2013. The date-reference chosen for Fig. 3 and throughout this contribution is Oct. 22, 2013, which is the onset of ground freezing. Starting from Nov. 26, 2013, the system only acquired 244 gradient-type configurations on the high-resolution section of the profile. These configurations were acquired six times per day, so that the number of daily measurements was reduced to 1464. The remote access and control of the resistivity meter

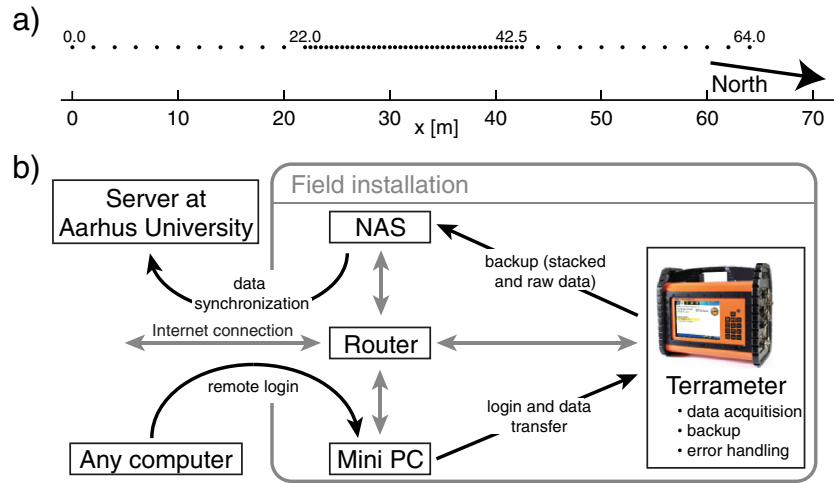


Fig. 2. (a) DC-IP field layout and (b) communication setup. (a) Sixty four electrodes were installed on a profile, with an inline electrode spacing of 0.5 m in the central part and 2 m towards the end of the profile. (b) The resistivity meter (ABEM Terrameter) is connected to a local network and the internet for fully automatic acquisition, data backup (to a network attached storage, NAS) and remote control.

over the internet was critically important to monitor the acquisition status and adapt the measurement sequences to the changing conditions. Once the sequence was reduced, the system smoothly acquired data until the end of the measurement period on Feb. 15, 2014.

3. DC-IP data processing and inversion methodology

3.1. Monitoring data and pre-processing

In order to be able to analyze a full time-series until February 2014, this study focuses on data that were acquired on the 0.5 m section of the profile with 42 electrodes. The full time-series consists of 1388 datasets, with 244 four-electrode configurations in each dataset. Each four-electrode configuration measurement consists of an apparent resistivity that—for a flat surface—is a weighted average of the resistivities below the electrodes. The depth penetration depends on the electrode spacing and the subsurface resistivity distribution, and the actual maximum depth of investigation can be determined after inversion of the data.

Apparent resistivity time-series are shown in Fig. 3c. The gray-shaded area marks the range of apparent resistivity values for all 244 measurement configurations and the black lines show the typical development for specific configurations. The shallow-sensing configurations (approximate depth of maximum sensitivity: 0.5 m) show an up to a hundred-fold increase in apparent resistivity after the onset of freezing. The increase in apparent resistivity is less pronounced for the deeper-sensing configurations and deepest sensing configurations (approximate depth of maximum sensitivity: 3 m) show no change that could be related to a freezing ground. This indicates that electrical resistivity only changes in the very shallow subsurface.

Variation of the IP decay curves in Fig. 4 also strongly depends on the electrode distances and corresponding sensitivity depth range. As for the apparent resistivities, the shallow-sensing configurations show the largest variation over time (Fig. 4a) and practically no variation can be observed for the deeper-sensing measurements (Fig. 4c). The observed variation for the shallow-sensing configuration (Fig. 4a) is a clear decrease in apparent chargeability with freezing of the ground.

Due to the high contact resistances larger than 100 kΩ after day 36, the acquisition system had problems with stabilizing the electrical current flow so that current switch-on times increased from less than 2 ms to more than 100 ms at the end of the acquisition period. DC data acquisition was not affected, but IP decays with such switch-on times can only be used if the exact—non-square—waveform is modeled in the inversion code. To our knowledge, no inversion code is currently available to invert time-domain IP data with arbitrary waveforms. Furthermore the long switch-on times may be an indication of capacitive coupling between the current and potential wires in the multichannel cables. For these reasons, we decided to focus on the IP data acquired until

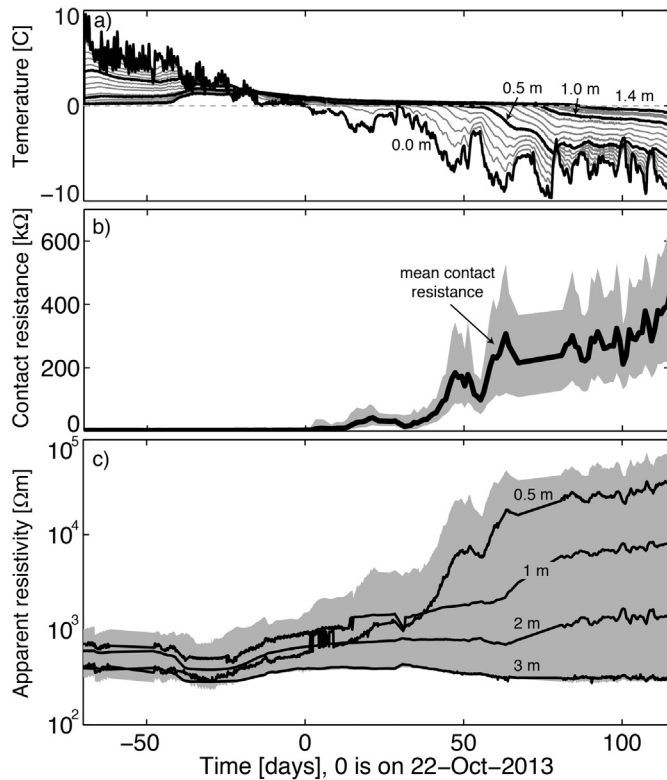


Fig. 3. Evolution of soil temperature (a), electrode contact resistances (b) and apparent resistivities (c) between August 2013 and February 2014. Contact resistances (b) increase with the initial freezing of the ground and continue to increase with decreasing soil temperature. Apparent resistivities (c) show a strong increase with freezing for shallow-sensing configurations, while configurations sensing the deeper subsurface (~3 m) show no increase with time. The labels in (c) indicate the distance between the potential electrodes for four specific measurements (0.5–3 m); for these measurements, the potential electrode distance is also approximately the depth of maximum sensitivity.

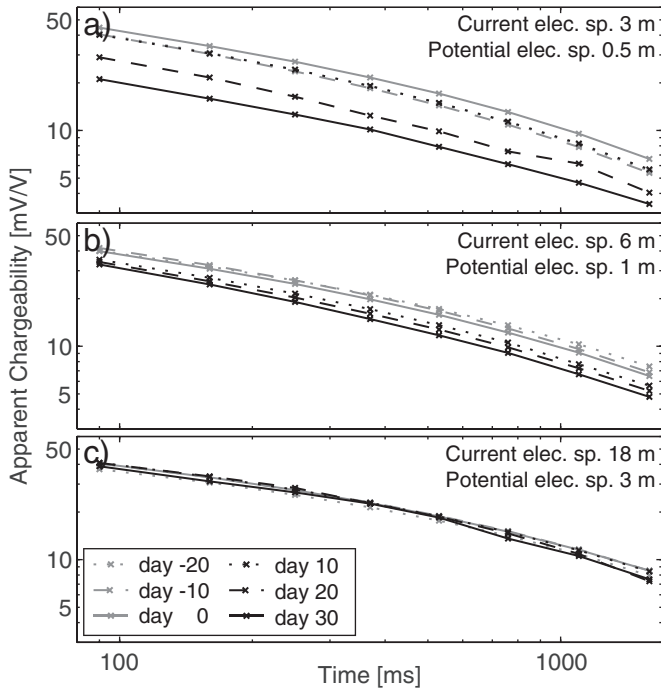


Fig. 4. Raw IP decays for three selected configurations with a current electrode spacing of 3 m (a), 6 m (b) and 18 m (c). The spacing of the potential electrodes is 0.5 m, 1 m and 3 m, respectively, and also corresponds to the approximate depth of maximum sensitivity. The shallow-sensing configurations show a clear decrease of apparent chargeability with time (and decreasing temperature), while the deep-sensing configurations show no significant temporal variation.

day 36 (Nov. 27). DC data were processed and inverted until day 115 (Feb. 15, 2014).

The data quality is very good and homogeneous throughout the dataset so that none of the DC-time-series or IP decays had to be removed. Inspection of full waveform data recordings for both current and potential measurements, sampled at 1 kHz, was performed on the entire dataset for checking data quality and allowed identification of decays with suspicious early-time acquisition: for some measurements, the earliest 2 out of 10 IP time-gates were affected by the finite current switch-on time of the system. These two early gates were therefore removed, but the other eight gates were kept because the full waveform data indicated good data quality. The remaining eight IP time-gates have center times of 85–1560 ms.

In another study, Doetsch et al. (2015) found that time- and location dependent data weighting was critically important to resolve small changes in their time-lapse DC-IP experiment. Here, several error estimation schemes were tested, e.g., including an absolute voltage error to account for the decreasing signal strength when contact resistances increase in response to freezing. In contrast to the experiment of Doetsch et al. (2015), our tests show that data quality is very homogeneous between different measurement configurations as well as very stable over time. Even inversions of data acquired after day 100, where contact resistances are very high (Fig. 3b), show the same final data misfit as inversions of pre-freezing data. Error differences between the four-electrode configurations are minimal, because only gradient-type measurements with a high signal-to-noise ratio are being inverted here. The DC error on the apparent resistivities was estimated as a 6% relative error. For the IP measurements, a combination of 10% relative error and 0.2 mV/V absolute error was used. The absolute error contribution for the first active gate is 0.5%, while the contribution to the last (eighth) gate is 6%. This higher relative error is due to the low signal level at the last gate of the IP decay. The combined relative and absolute data error was used for weighting the data in the inversions.

3.2. Cole–Cole model

Typical inversions of time-domain IP data (e.g., Oldenburg and Li, 1994) use the DC apparent resistivity data and the integral chargeability, i.e. the chargeability integrated over all time-gates, to retrieve the subsurface resistivity and chargeability distribution. These inversions neglect the frequency information contained in the shapes of the IP decay curves. Inversion of time-domain full-decay IP data (Fiandaca et al., 2012, 2013) uses the entire IP decay along with the DC measurements to invert for parameter distributions that explain the data. These parameters should be able to describe the decay behavior of the IP measurements along with the apparent resistivities.

Here, we use the Cole–Cole model (Cole and Cole, 1941; Pelton et al., 1978) that uses four parameters to characterize the soil impedance and its frequency dependence. It has been widely applied both for spectral IP analysis (e.g., Loke et al., 2006; Yoshioka and Zhdanov, 2005) and in time-domain IP inversions (e.g., Hönl and Tezkan, 2007; Yuval and Oldenburg, 1997). We parameterize the complex resistivity ζ_j in each cell j in the 2D parameter mesh as (Pelton et al., 1978)

$$\zeta_j(\omega) = \rho_j \left[1 - m_0 \left(1 - \frac{1}{1 + (i\omega\tau_j)^c} \right) \right], \quad (1)$$

where ρ is the DC resistivity, m_0 is the intrinsic chargeability, τ is the time constant, c is the frequency exponent and i is the imaginary unit. In the combined DC-IP inversions, we invert for all four parameters simultaneously. For the interpretation, we also show the normalized chargeability m_0/ρ , as it is more closely related to the polarization characteristics of the ground than m_0 .

3.3. Combined DC-IP inversion method

Both DC-only and combined DC-IP inversions were carried out in 2D using the inversion software AarhusInv (Auken et al., 2014; Fiandaca et al., 2012, 2013), where the DC-IP models are parameterized using the above-described Cole–Cole model. For DC-only inversions, only the subsurface resistivity distribution is estimated. For combined DC-IP inversions the full IP decays are added to data space for inverting one parameter field for each of the four Cole–Cole parameters. The combined DC-IP modeling takes into account the current waveform (in terms of sequence of square pulses) in the forward response, in order to avoid bias in the parameter estimation (Fiandaca et al., 2012, 2013). The combined DC-IP inversions start by inverting the DC-data only; after a few iterations, IP data are added and all parameters are inverted simultaneously.

The finite-element parameter mesh for the inversion is built using the GPS-derived topography and electrode positions with a lateral cell spacing of 0.5 m, which corresponds to the electrode spacing. Vertical discretization was chosen to include 20 layers, with a layer thickness of 0.14 m at the surface and increasing thickness with depth. This parameter mesh is refined in the forward modeling, for increased accuracy.

The regularization that is implemented in the inversion algorithm to stabilize the inversion includes vertical and horizontal smoothing as well as damping towards a prior model. A focusing scheme (Vignoli et al., 2015) is available for the a priori regularization so that the strong expected resistivity changes that occur with freezing of the ground are allowed. The minimum-support focusing scheme promotes changes of only few cells, but once a cell shows variation, there are only weak constraints on the magnitude of change. Similarly to what is shown in Vignoli et al. (2015) for the vertical/horizontal regularization, the objective function minimizes

the prior misfit defined as:

$$\Phi_{\text{prior}}(\mathbf{m}-\mathbf{m}_0) = \sum_i \frac{(m_i-m_{0i})^2}{(m_i-m_{0i})^2 + \sigma_i^2} \quad (2)$$

In Eq. (2), the symbol σ_i represents a threshold value, expressed as a fraction of reference parameter values (3% in our filed example): $\frac{(m_i-m_{0i})^2}{(m_i-m_{0i})^2 + \sigma_i^2}$ tends to 1 when $|m_i - m_{0i}| \gg \sigma_i$, while $\frac{(m_i-m_{0i})^2}{(m_i-m_{0i})^2 + \sigma_i^2}$ tends to 0 when $\sigma_i \gg |m_i - m_{0i}|$. Consequently, the minimum support functional “counts” the number of model parameters that differ more than the σ_i threshold, regardless of the magnitude difference.

For time-lapse inversions the prior model can be the baseline inversion result that was calculated from data recorded prior to the expected changes. The horizontal and vertical smoothing can either be applied to the full model or the model update from the prior model. The option of applying the smoothing to the model update is especially important when inverting for small changes over time.

4. DC-IP inversions and results

4.1. DC inversions

In order to cover the full time range until February 2014, we invert all direct-current (DC) data without considering the IP decays. We first invert the dataset of day 0 (Oct. 22, 2013) that marks the last day before the freezing of the ground begins. For the inversion of all other datasets, the day 0 inversion result (Fig. 5b) is used as start and prior model. Regular L2 smoothing (standard deviation of 0.2 in vertical and 0.1 in horizontal direction) was chosen on the full model and a focusing scheme (see Section 3.3) is used for the a priori regularization.

No time-lapse data correction is applied. While other studies with small time-lapse changes found that data correction strongly improves inversion results (e.g., Doetsch et al., 2012; LaBrecque and Yang, 2001), this is not necessary for the dataset discussed here. Up to hundred-fold increases in apparent resistivities (see Fig. 3c) give such a strong signal that no special data treatment is necessary.

A total of 1388 datasets, with 244 measurements each, are inverted, covering the time from July 2013 to Feb. 2014. All inversions converge within three to six iterations to a normalized data

misfit (weighted by the estimated error) of 1–1.7, indicating an RMS misfit of 6–10%. Along with the inversions, we calculate the depth of investigation (DOI) for all models, using the formulation of Christiansen and Auken (2012), but including correlations between the IP parameters in the computation (Fiandaca et al., 2015). The DOI is included in all model plots by partially shading poorly resolved areas and fully blanking unresolved model areas. Fig. 5 shows four selected inversion results, two before freezing started and two with partially frozen soil. The unfrozen resistivity distribution shows low resistivities at the surface (<400 Ωm), intermediate resistivities of 1000–2000 Ωm between 0.5 and 2 m depth and low resistivities (<200 Ωm) below. No prior information is available about a lithological transition at 2 m depth that justifies the resistivity decrease, but between 2 and 3.5 m the temperature measurements at the MET station (30 m west of the profile) show that temperatures are between 0 °C and 1 °C year-round (Fig. 1c). Above-freezing temperatures and low resistivities suggest the presence of water flow in the loose sediments that is fed by isothermal springs located North (uphill) of our field site.

Shallow resistivities strongly increase with the freezing of the ground (Fig. 5c and d), in many places by more than a factor of 100. The resistivity of the shallowest 0.5 m in unfrozen state shows inhomogeneity (resistivity around $x = 34$ m is higher than elsewhere), due to local variations in material composition and soil moisture. This inhomogeneity also exists at day 50, while the day-100 image (Fig. 5d) shows a homogeneously high resistivity in the top 0.5 m. The bottom of the high-resistivity layer (~4000 Ωm, white color, in Fig. 5c and d) is practically flat, indicating a flat freezing front.

The vertical resistivity profiles at the location of the temperature sensors (marked in Fig. 5) are extracted from all 1388 inversion results and are shown in Fig. 6, along with the co-located temperature measurements. Comparison of the temperature measurements at the DC-IP profile (Fig. 6a) and at the MET station (Fig. 1c) in 30 m distance shows that the general time development of the temperature with time and depth is very similar. However, there are differences in the near-surface temperature variations. Diurnal variations penetrate to a depth of up to 0.5 m at the MET station, but can only be observed to 0.1–0.2 m at the DC-IP profile. In contrast, the reduction in freezing depth around day 30 can only be observed at the DC-IP profile. Before the onset of freezing (before day 0), resistivities are mostly a function of soil moisture. The decrease of resistivity (red colors at depth) along the entire depth range at day –40 is the result of a large rain event that fully saturated the soil. The downward migration of the water also transported significant amounts of heat energy through the system, increasing the temperature below 0.5 m depth and decreasing the temperature in the very shallow subsurface.

With the onset of freezing, temperature decreases and resistivity increases from the surface downwards. For the first 30 days of freezing, temperatures stay relatively mild, the freezing horizon fluctuates between 0 and 0.2 m depth, and resistivities decrease only in the top layer. Starting from day 30, temperatures decrease significantly, steadily pushing the freezing horizon down (Fig. 6a). This decrease in temperature causes the resistivity to increase strongly from the surface downwards. While there is a clear correlation between the development of temperature and resistivity in Fig. 6, it is not possible to define a single resistivity that defines the transition from unfrozen to frozen ground. The resistivity below 2.5 m depth is completely unaffected by the freezing of the shallow soil (see Fig. 5c and d), probably because of the water flow from the isothermal springs that buffers the temperature.

4.2. DC-IP baseline inversion

For the combined DC-IP inversions, the same day 0 baseline dataset was chosen as for the DC-only inversions, only that the IP decays are now included. The baseline inversion uses no a priori constraints and the same vertical and horizontal smoothing as in the DC-only inversions

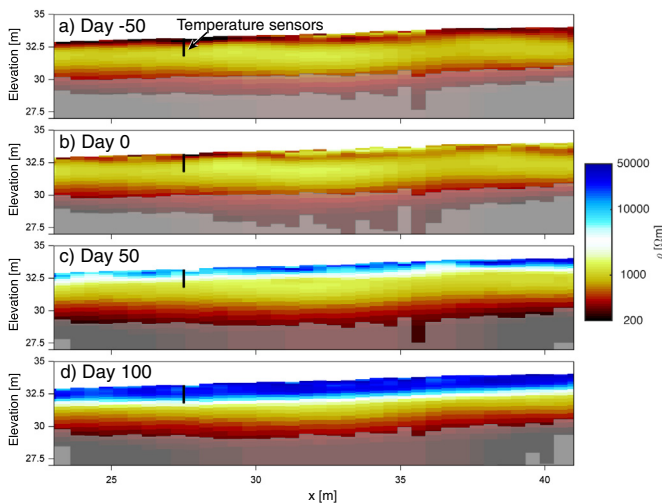


Fig. 5. DC inversion result for data collected on Sept. 2 (a, day –50), Oct. 22 (b, day 0), Dec. 11, 2013 (c, day 50) and Jan. 30, 2014 (d, day 100). Onset of freezing is around day 0. The black line at position $x = 27.5$ m marks the borehole with temperature sensors. Strong subsurface resistivity changes can be observed in the 2 m below surface level, while the resistivity values below stay constant. Shading indicates the depth of investigation with light shading indicating regions that are poorly constrained by the data and fully shaded areas not being constrained at all.

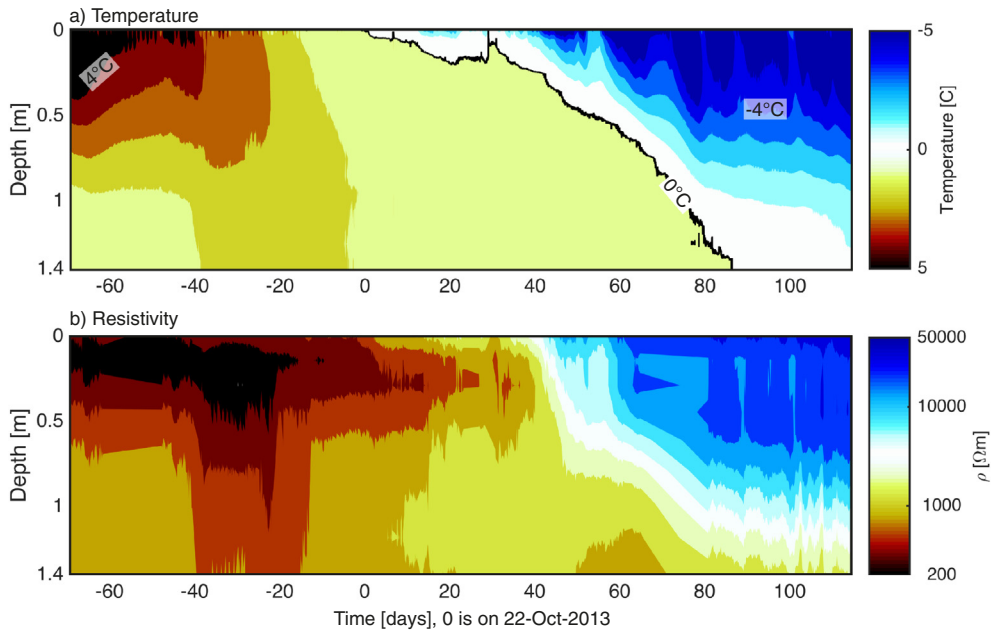


Fig. 6. Plots of (a) temperature and (b) resistivity at the borehole on the DC-IP profile as a function of time and depth. The black line in the temperature plot indicates the freezing (0°C) depth. Resistivity and temperature show a clear correlation, but it is not possible to directly translate resistivity into temperature. The temperature development at the DC-IP profile (a) shows less diurnal variations than at the MET station (Fig. 1c); the reduction in freezing depth around day 30 is only occurring at the DC-IP profile.

(standard deviation of 0.2 and 0.1, respectively) are used. The inversion converges in three DC-only and eight combined DC and IP iterations to a normalized RMS misfit of 1.8 for the DC data and 1.0 for the IP data. Fig. 7 shows the four Cole-Cole parameters for the baseline inversion result.

Not surprisingly, the resistivity model ρ (Fig. 7a) is practically identical to the DC-only result in Fig. 5b. Chargeability m_0 (Fig. 7b) and normalized chargeability m_0/ρ (Fig. 7e) show strong variations in the top 30–50 cm and intermediate values between 0.5 and 1.5 m depth. Both chargeability and normalized chargeability show high values of up to 200 mV/V and 1 mS/m, respectively, below 1.5 m depth. Unfortunately the models are not fully resolved below about 1.5 m depth (as indicated by the white shading), as this area is below the depth of investigation. Nevertheless, the higher normalized chargeability below 1.5 m depth is an indication of a higher polarizability of the material at that depth. The basaltic deposits present at the field site contain magnetite, which exhibits a strong IP signature (e.g. Abdel Aal et al., 2014; Hubbard et al., 2013b; Slater et al., 2006) and can explain the polarizability values. Slater et al. (2006) presented normalized chargeability values of saturated magnetite/sand mixtures ranging from 3 to 70 mS/m, when varying the magnetite concentration from 5% to 100% in weight. Hence the 1 mS/m value below 1.5 m is compatible with a magnetite concentration of a few percent in weight. The lower normalized chargeability values above 1.5 m depth can be due to a decrease in saturation. This interpretation is in partial accordance with the findings of Ulrich and Slater (2004), who found normalized chargeability values increasing with saturation in unconsolidated sands.

The time constant τ is also shortest near the surface (0.2 s) and shows values of 0.5 s below 1.5 m depth in the area where chargeability is higher. Both the mineral grain size and the electrolyte concentration control the values of the time constant, and Slater et al. (2005) found that the normalized time constant $\tau_n = \tau/\rho$ removes most of the effect of changes in electrolyte concentration. No information is available about the dimension of the magnetite grains at the field site, but the range of normalized time constant τ_n found in the baseline model (0.17–0.60 s·mS/m) is in accordance with the results of Hubbard et al. (2013b) for a magnetite/sand mixture (crushed magnetite single crystals sieved to 1–2 mm with a flaky and angular morphology) at the slightly acidic pH values present at the site (i.e. 0.25–0.63 s·mS/m with

pH ranging from 6.3 to 7 and redox reactions occurring at the magnetite surface).

The frequency exponent c shows relatively little variation, with slightly higher values close to the surface, which indicate a narrower frequency distribution. There is significant lateral variability in the polarization characteristics of the shallow-most layer. The soil around the temperature sensors ($x = 27.5$ m) is quite polarizable (high m_0/ρ), while it has very low polarization characteristics around $x = 34$ m (low m_0/ρ).

4.3. DC-IP time-lapse inversion

The time-lapse DC-IP inversions span the time from days –20 to 36, with respect to Oct. 22, 2013. The DC-IP baseline model (Fig. 7) is used as reference and starting model, so that the inversion calculates parameter changes from the baseline model. The L2 smoothing regularization is only applied on the update to the baseline model. The a priori regularization uses a focusing scheme (Section 3.3) that promotes changes of only few cells, but once a cell shows variation, there are only weak constraints on the magnitude of change. As for the DC-only inversions, no time-lapse data corrections were applied. With contact resistances dramatically changing, the assumption of large static errors compared to the time-varying error sources is not fulfilled. Even for circumstances where time-lapse corrections improve inversions of DC data, Doetsch et al. (2015) found that time-lapse corrections only give marginally better results for IP inversions. Inversions of all 360 time steps converge within three to five DC-only and four to eight combined DC-IP iterations to a normalized RMS data misfit of 1.0–1.7 both for the DC and the IP data component.

Fig. 8 shows a sample inversion result (day 28) as ratios of the time-lapse model and the baseline result of Fig. 7. A value of 1 (white color) corresponds to no change in the respective parameter. Please observe the different color scales and ranges, where blue corresponds to an increase in resistivity ρ and a decrease in chargeability m_0 , time constant τ , frequency exponent c and normalized chargeability m_0/ρ . Resistivity clearly increases in the topmost meter along the full profile, but there is also some variation along the profile. Increases are detected down to 2 m in the center of the profile, while other places only show an increase down to 1 m depth. The m_0 section indicates a decrease in

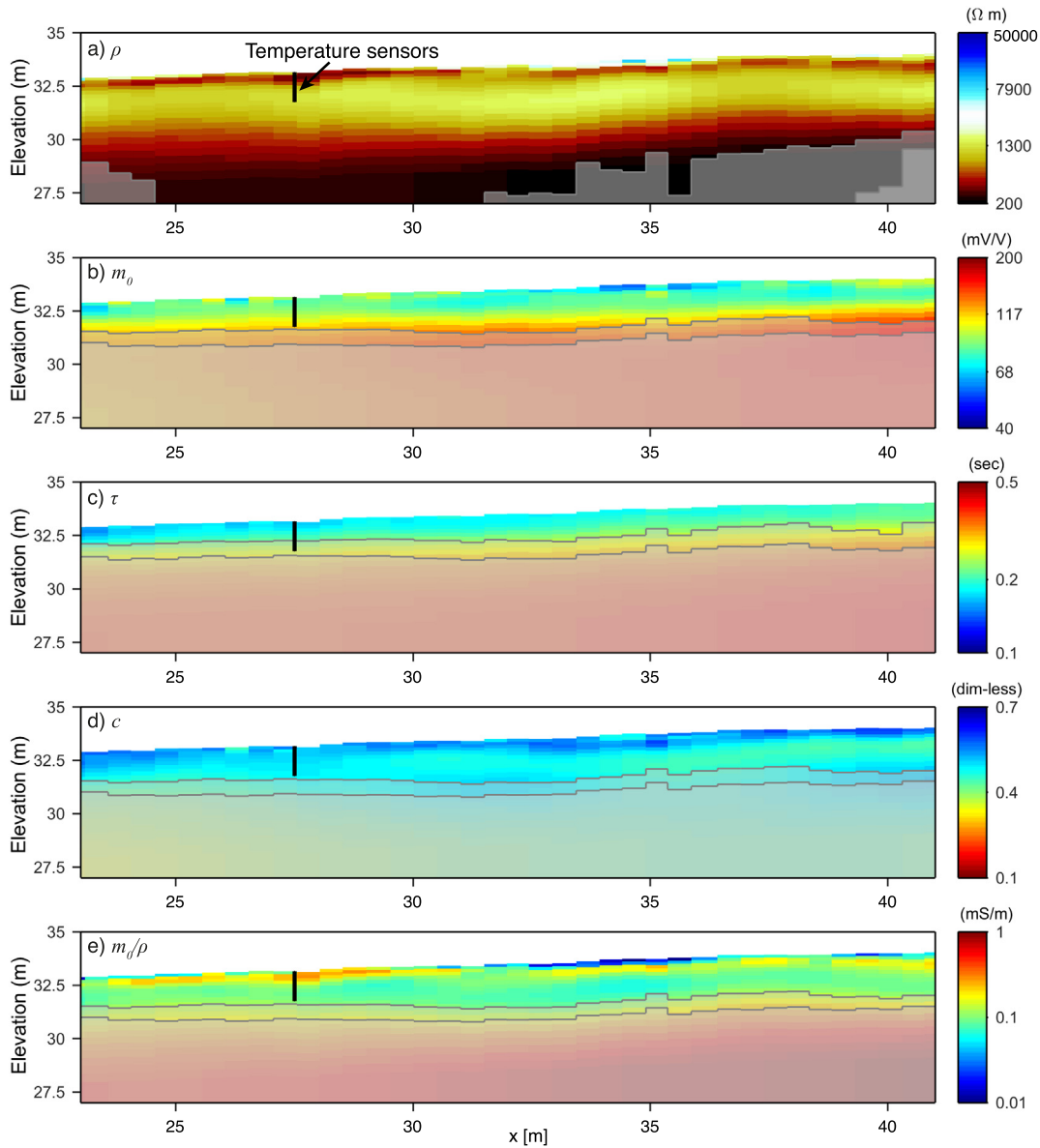


Fig. 7. Baseline DC-IP inversion result of the data collected at the onset of freezing (Oct. 22, 2013). Resistivity ρ (a) shows high resistivities ($>500 \Omega\text{m}$) down to about 3 m depth and lower resistivities below. Chargeability m_0 (b), normalized chargeability m_0/ρ (e) and decay constant τ (c) are low in the most shallow 0.5 m and increase below. The frequency component c (d) shows little overall variation. Shading indicates the depth of investigation.

chargeability that is laterally consistent along the full profile, but only affects the top 0.5 m. Changes in τ and c are less pronounced (observe the different color scale range), with c showing a decrease at the same location as m_0 . The strongest change (observe the difference color range) can be observed in normalized chargeability m_0/ρ , as the increase in resistivity and decrease in chargeability multiply. The change in m_0/ρ varies along the profile, with m_0/ρ only decreasing the topmost 0.5 m in some places, while changes extending to ~ 1.5 m in others.

The inverted changes in the Cole–Cole parameters at the location of the temperature sensors were extracted from the 360 inversion results and are shown as a function of time in Fig. 9. These images show how temperature and the Cole–Cole parameters at this specific location ($x = 27.5$ m) develop over time. They are highly consistent, especially considering that the models are constrained towards the same baseline, but not to the previous or following time-lapse inversion model. Before the onset of freezing, ρ and m_0/ρ show strong variation (Fig. 9b and f) due to water saturation fluctuations in the soil,

while m_0 and the other IP parameters are affected much less by these changes. Once the topmost soil layer freezes, resistivity of the most shallow resistivity cell increases and the thickness of the high-resistivity zone increases with time. Especially after day 15, the increase in ρ extends deeper than the freezing depth indicated in the temperature plot (Fig. 9a). The shallow decrease in chargeability that is visible in the raw data (Fig. 4a) is also evident in the inversion results. The reduction of chargeability (Fig. 9c) is clear and consistent, but not as strong as the increase in resistivity. While the resistivity increase extends below 1 m depth, the chargeability decrease is concentrated in the top 0.5 m. Normalized chargeability m_0/ρ (Fig. 9e) shows the combined effect of the increase in resistivity and decrease in chargeability. Changes in normalized chargeability are therefore stronger (4-fold decrease instead of 2-fold) and span the same depth range as the changes in ρ . The strongest decrease is however limited to the top 0.5 m, where ρ shows a strong increase and m_0 a strong decrease. The time constant τ (Fig. 9d) reduces right after the beginning of freezing, but shows a less clear trend at

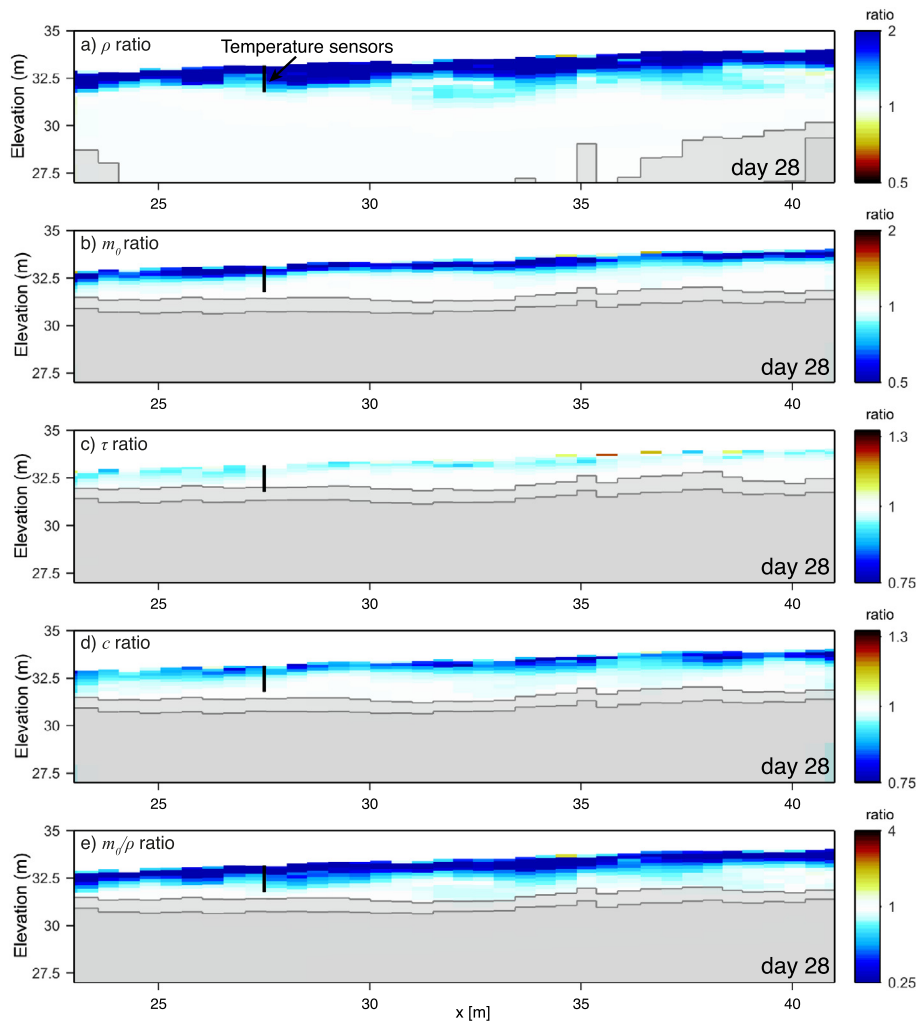


Fig. 8. DC-IP time-lapse inversion results for day 28 (Nov. 19, 2013), normalized by the baseline inversion result (Fig. 5). The freezing of the shallow soil is evident as an increase in resistivity ρ (a) and a decrease in chargeability m_0 (b). The frequency component c (d) also decreases, indicating a wider frequency range, while the decay constant τ (c) shows very little variation. The strongest decrease (observe the different color scales) is found for the normalized chargeability m_0/ρ (e), as the increase in resistivity and decrease in chargeability multiply. Shading indicates the depth of investigation.

later times. The decrease in c (Fig. 9e) has a similar depth extent as m_0 , but c only decreases by 1/5 while m_0 decreases by a factor of 2.

5. Discussion and interpretation

5.1. Resistivity controlled by freezing

For the interpretation of the inversion results, it is important to understand the freezing process in partially saturated soil and sediments (e.g., Anderson and Morgenstern, 1973; Hoekstra et al., 1975). When partially saturated soil freezes, the pore water starts to freeze at the air-water interface, building ice crystals. The ice crystals contain practically no ions, so the number of free ions in the remaining pore water increases. When temperatures decrease, more water freezes so that the ice crystals fill up more pore volume and ion concentration in the unfrozen water increases further. The unfrozen water builds an interfacial zone between the ice and the grain surfaces. This interfacial water layer thins out when the temperature decreases, but does not disappear completely at environmental temperatures. According to Anderson and Morgenstern (1973) it might only be 5–10 Å thick at -10 °C and it contains ions both from the previously free soil water and the grain surfaces. These ions act as electrical charge carriers when an electrical field is applied.

Sediment grains are typically insulators so that electrical conduction is restricted to the pore water and the grain surfaces. In the quartz-rich sediments on Disko Island, surface conductivity plays a minor role when the ground is unfrozen and electrical conductivity is mostly a function of soil moisture and water conductivity. When the ground starts to freeze, electrical conduction is limited to the interfacial layer between ice crystals and grain surfaces. This increases the bulk resistivity of the ground, which becomes larger as the unfrozen interfacial layer thins.

The resistivity of unfrozen and frozen soil depends on lithology (rock type), porosity and soil moisture (see e.g., Hoekstra et al., 1975). Direct translation between resistivity and (below freezing) temperature is therefore not possible, as illustrated by Fig. 6 (no resistivity contour tracks the 0 °C contour). The variation of temperature and resistivity as a function of depth can be appreciated in Fig. 10a and b. At day 0, temperature is 0 °C at the surface and slightly above 0 °C below, while resistivity varies strongly with depth. When interpreting the resistivity variation in response to temperature changes, the depth variation of resistivity at a constant temperature should be taken into account. As temperatures at day 0 are close to 0 °C at all depths, only differences to the day 0 resistivity line in Fig. 10b should be interpreted. Temperature shows the largest time variation at the surface, both before and after the onset of freezing. Resistivity only varies mildly before

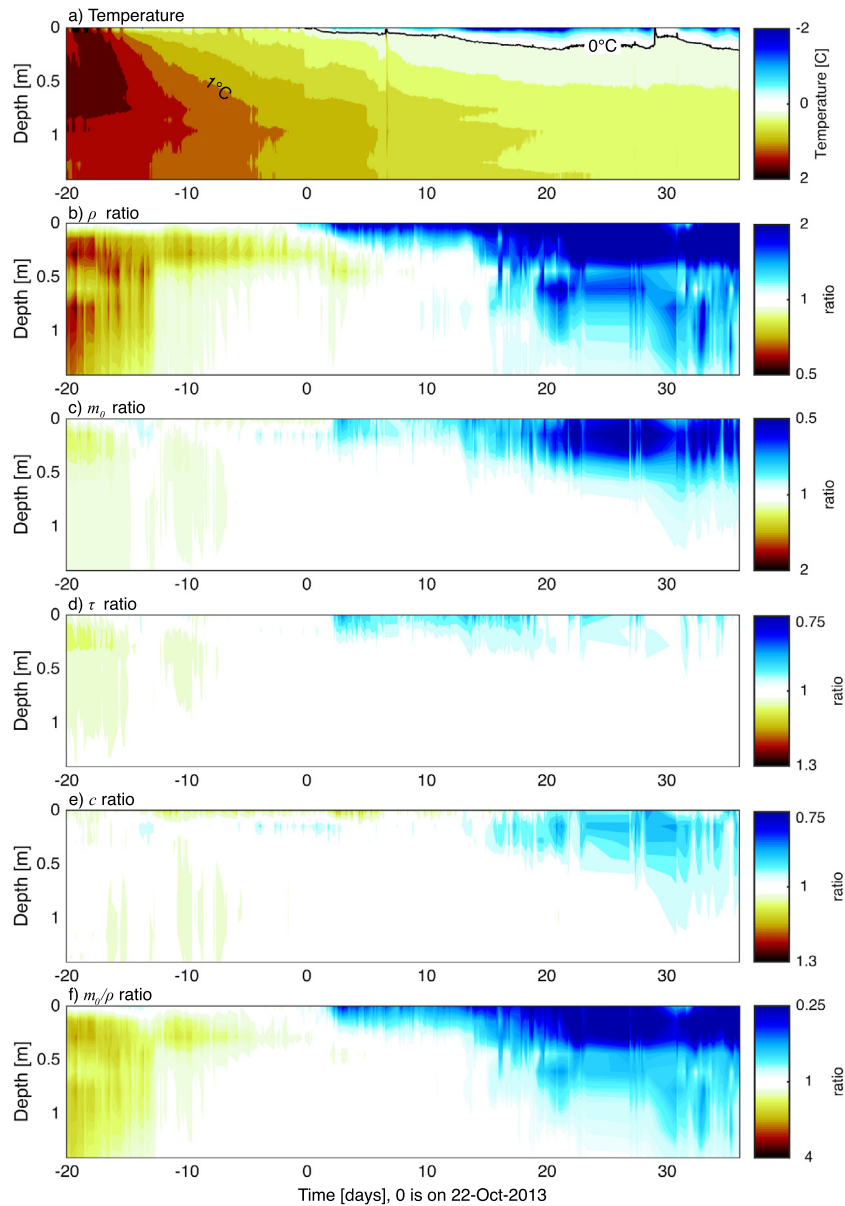


Fig. 9. Plots of temperature (a), ρ (b), m_0 (c), τ (d), c (e) and m_0/ρ (f) variation as a function of time and depth. The black line in the temperature plot indicates the freezing (0°C) depth. m_0/ρ shows the strongest change with the freezing of the ground, being an accumulation of the changes in ρ and those in m_0 .

the onset of freezing, but increases strongly after day 0. The resistivity variation is strongest at the surface, but extends down to 2.5 m depth.

Plotting resistivity against temperature in a scatter plot can reveal a relationship between the two parameters. Fig. 10c shows that there is a strong increase of resistivity around 0°C , followed by an increase that is consistent with an exponential relationship between resistivity and temperature (linear relationship between the logarithm of resistivity and temperature). This is the behavior predicted for saturated sand and gravel by Hoekstra et al. (1975) and confirmed by others (e.g., Hauck, 2002). The immediate increase of resistivity around 0°C shows that ion concentration in the pore water is small and that many large pores exist. In these pores, water can freeze rapidly at 0°C , until the ion concentration in the remaining unfrozen water increases, depresses the freezing point and builds the interfacial layer. After the initial strong increase in resistivity at 0°C , the further increase approximately follows an exponential relationship between resistivity and temperature.

5.2. The effect of freezing on induced polarization

The IP inversions image the low-frequency capacitance of the soil, which is caused by the electrical double layer on the surfaces of the grains (see e.g., Slater et al., 2006 for metal–sand and clay–sand mixtures and Revil et al., 2012 for a review of IP mechanisms in general). When the initial ice forms in the center of the pores, the electrical double layer is only weakly disturbed so that the change in normalized chargeability is relatively small (see days 0–10 in Fig. 9f). When temperature decreases further and less unfrozen water is available, the electrical double layer is part of the unfrozen interfacial water layer described above. With the thinning of the interfacial layer, the electrical double layer is also affected and eventually disappears. Additionally, the increased amount of ions in solution contributes to the thinning of the double layer (Slater et al., 2005) and decreases the mobility of the polarizable charges (Lesmes and Frye, 2001). The thinner interfacial layer and the increase in ion concentration both lead to a smaller chargeability. This decrease in normalized chargeability is evident in Fig. 9f, being stronger from day 15.

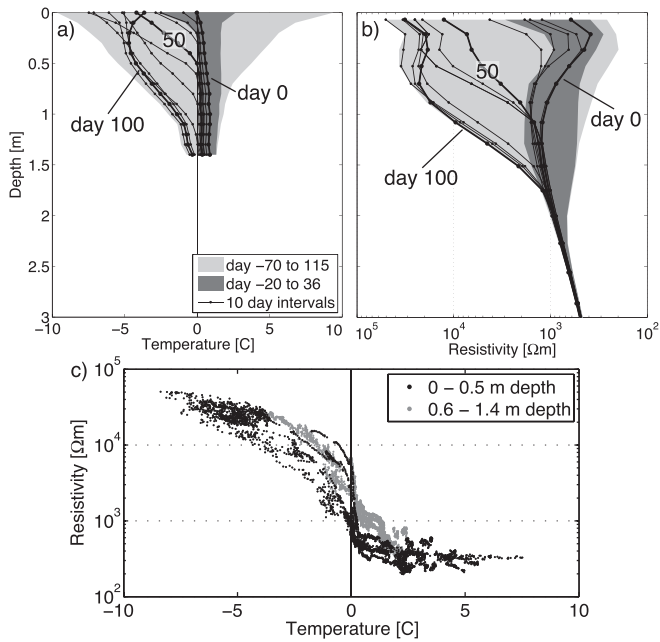


Fig. 10. Vertical temperature (a) and resistivity (b) profiles for the entire survey time (light grey area), time around the onset of freezing (dark shaded area) and every 10 days between days 0 and 110 (Oct. 22, 2013 to Feb. 9, 2014). (c) shows a scatter plot of resistivity and temperature that illustrates the strong increase of resistivity at 0 °C and a further increase with decreasing temperature.

A decrease of chargeability and normalized chargeability with soil freezing was also measured with frequency-domain spectral induced polarization in the laboratory on Arctic soil samples by Wu et al. (2013). Compared to our results, a greater depletion of the IP signature with freezing and temperature decrease was observed in the laboratory study, but it should be noted that in our experiment from day –20 to day 36 the temperature decreased only down to –2 °C in the first few tens of centimeters and a complete sediment freezing probably was not reached. The decrease in pore size and interfacial layer thickness also leads to a smaller diffusion length and a resulting decrease in the decay length (time constant) τ (Fig. 9d), again in agreement with the findings of Wu et al. (2013) for the laboratory freeze–thaw experiments on Arctic soils. The frequency exponent c shows no clear signal for the first 13 days and clearly decreases at later times. This decrease in c implies a wider frequency distribution for the IP decays, which could indicate a wider distribution of pore sizes or interfacial layer thicknesses. The decrease in both m_0 and c may explain the less pronounced

decrease in τ after day 30, because τ variations are not resolved due to the smaller sensitivity to τ with smaller c (wider distributions) and smaller m_0 values (lower signal to noise ratio).

The vertical profiles of temperature and change in resistivity and chargeability for days –20 to 36 (Fig. 11) show that chargeability m_0 is almost unaffected by temperature and other factors (e.g., soil moisture) before freezing starts (light grey area in Fig. 11c), probably because these factors affect the bulk and surface conductivity in a similar way and are canceled out. Once freezing commences, changes in chargeability are observed to about 0.8 m depth, even when the temperature sensors measure the freezing depth at 0.2 m. Changes in resistivity (Fig. 11b) extend even deeper. Although this might be caused partly by the smooth inversions, it shows that resistivity and chargeability also change below the freezing horizon. For our study, chargeability m_0 is a better proxy for tracking the onset of the freezing than resistivity and normalized chargeability, as also suggested by Wu et al. (2013) in their laboratory study when comparing phase response and imaginary conductivity.

The IP measurements and inversion results presented above show a clear signature of the freezing. But more controlled laboratory experiments on soil samples from the field site seem important to understand further the sources of the observed IP changes. The observed changes in parameters during the 36-day freezing period that was monitored with IP are much smaller than the expected changes during a full winter season. Resistivity increased by a factor of 4 in the first 36 days of freezing, while the increase after 100 days was more than 100-fold.

5.3. Detecting and characterizing lateral variability

One of the main advantages of DC-IP surveys and semi-permanent monitoring installations is the sensitivity to lateral variations that is achieved with minimal disturbance of the subsurface. Lateral variations are clearly visible in Figs. 5, 7 and 8, as discussed above. Nevertheless, lateral variation is minimal for this field example, due to the chosen location and direction of the profile. While the field site is flat, there is a topographic gradient towards Disco Bay in the south. Our profile is oriented parallel to this topographic gradient, and it is located in the most homogeneous section of the sedimentary fan. More variability would be expected on a West–East profile along a topographic contour, where possible underground streams and soil moisture variations might result in lateral variations of the freezing depth. This study has shown that DC-IP data can be reliably acquired in this rough environment and should now be used at field sites with more heterogeneity and topography. In these environments, DC-IP monitoring could play a major role in understanding landscape control on the freeze–thaw cycle and permafrost thawing. Thawing and release of water and ions may be more

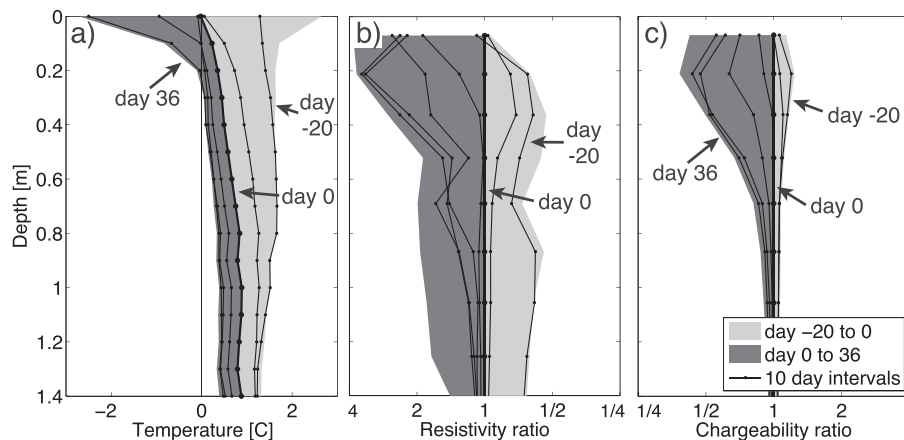


Fig. 11. Vertical profiles of temperature (a), change in resistivity (b) and change in chargeability (c). Resistivity and chargeability are normalized by the pre-freezing values so that values >1 indicate an increase, values <1 indicate a decrease in resistivity/chargeability.

pronounced in drier and more well-drained parts of the landscape than in low lands. Landscape intergradation is of key interest in order to assess the net effect of climate changes, including annual freeze–thaw cycles. In this context DC-IP data provide new opportunities in gaining high-resolution information on fluxes on a landscape scale.

5.4. Acquisition system

There are special demands for the acquisition system to work in a harsh environment, and the stability and reliability of the hardware is core to a successful long term and almost unattended monitoring.

With contact resistances of 500 k Ω and above, and typical maximum injection voltages of 600 V, the resulting injection currents are 0.6 mA and below. These small injection currents are very difficult to stabilize. The resulting measured voltages are also very small and have to be measured through the high contact resistances of the potential electrodes. The high contact resistance is particularly problematic for the IP measurements, and separate cables for current injection and potential measurements may be needed for decreasing the capacitive coupling of the current and potential wires. The stress and quality demands on an acquisition system in Arctic conditions are therefore very high, especially to the power supply and the current injection unit. Remote monitoring and control of our acquisition system through an internet connection were critically important to adjust the monitoring frequency, measurement protocol, and acquisition parameters, when environmental conditions and system status changed.

6. Conclusions

Seven months of DC-IP data were recorded for active layer monitoring in western Greenland. The DC data are of high quality for the entire 225 days and shallow-sensing electrode configurations measured a hundred-fold increase in resistivity with freezing, while deep-sensing measurements were unaffected by the temperature change. IP data were recorded over the full time range, but only data for the first 36 days of freezing could be analyzed as data recorded later were affected by current injection problems due to high electrode contact resistances. Our monitoring setup allowed for remote control of the data acquisition system in response to changes in the system performance due to the increasingly difficult conditions during the freezing period in the winter. This ability to interactively change the measurement schedule was critically important in order to record data during the time of very high (> 100 k Ω) electrode contact resistances.

The DC inversion results show a strong increase in resistivity with freezing and the depth of strong increase agrees with the freezing depth measured by temperature sensors. For below-freezing temperatures we confirm an exponential relationship between resistivity and temperature that was previously suggested in the literature. However, it is not possible to directly convert resistivity or changes in resistivity to temperature variations. Resistivity is a function of porosity, water content, pore water salinity, and temperature and it is difficult to disentangle these effects. IP measurements can help to separate the time-lapse variations, by adding complementary information. We find a decrease in normalized chargeability of the freezing soil, related to the thinning of the electrical double layer. A decrease in the time constant is also observed, which we interpret as the result of a shorter diffusion length due to the decreased average particle or pore size of the frozen material. Furthermore, we find that the non-normalized chargeability m_0 is a better proxy for tracking the freezing onset compared to normalized chargeability and resistivity. Surface and bulk conductivity are similarly affected by temperature and other factors (like soil moisture) before freezing, but this influence partly cancels for m_0 , which depends on the ratio of surface and bulk conductivity.

Our results show that time-lapse DC-IP measurements and inversion can be used to non-intrusively monitor the active layer freezing processes at a scale of tens to hundreds of meters. Future investigations

could include calibration with laboratory measurements and coupling of the DC-IP inversions with simulators for heat conduction and flow and transport in freezing soils. Fully coupled inversions that integrate the DC-IP data along with temperature and soil moisture data and solve for thermal and flow parameters could help to disentangle complex processes—such as water flow, water freezing, heat conduction and increase in ion concentration—that occur during the freezing of soil. DC-IP monitoring could play a major role in understanding these freezing processes and monitor the state of the active layer on a relevant space and time scale.

Acknowledgements

Funding for this study was provided to BE by the Danish National Research Foundation (CENPERM DNR100) and is part of a larger research program at 10 sites in Greenland. The authors would like to thank technician Simon Ejlertsen for his support in building the monitoring system and Charlotte Sigsgaard for compiling the weather data. Thanks to the Arctic Station (<http://arktiskstation.ku.dk>) for supplying data and providing the logistical platform as well as permits. J. Doetsch was partly funded by the Swiss Competence Center for Energy Research—Supply of Electricity (SCCER-SoE) and partly by internal funds from the HydroGeophysics Group at Aarhus University. Reviews from L. Slater and two anonymous reviewers have helped to improve the clarity of this paper.

References

- Abdel Aal, G.Z., Atekwana, E.A., Revil, A., 2014. Geophysical signatures of disseminated iron minerals: a proxy for understanding subsurface biophysicochemical processes. *J. Geophys. Res. Biogeosci.* 119. <http://dx.doi.org/10.1002/2014JG002659> (2014JG002659).
- Anderson, D.M., Morgenstern, N.R., 1973. *Physics, chemistry, and mechanics of frozen ground: a review. Permafrost: The North American Contribution to the Second International Conference. National Academy of Sciences, Washington, DC*, pp. 257–288.
- Anisimov, O.A., Nelson, F.E., 1996. Permafrost distribution in the Northern Hemisphere under scenarios of climatic change. *Glob. Planet. Chang.* 14 (1–2), 59–72.
- Auken, E., Christiansen, A.V., Kirkegaard, C., Fiandaca, G., Schamper, C., Behroozmand, A.A., Binley, A., Nielsen, E., Effersø, F., Christensen, N.B., Sørensen, K., Foged, N., Vignoli, G., 2014. An overview of a highly versatile forward and stable inverse algorithm for airborne, ground-based and borehole electromagnetic and electric data. *Explor. Geophys* <http://dx.doi.org/10.1071/EG13097>.
- Christiansen, A.V., Auken, E., 2012. A global measure for depth of investigation. *Geophysics* 77, WB171–WB177. <http://dx.doi.org/10.1190/geo2011-0393.1>.
- Cole, K.S., Cole, R.H., 1941. Dispersion and absorption in dielectrics: I. Alternating current characteristics. *J. Chem. Phys.* 9, 341–351. <http://dx.doi.org/10.1063/1.1759096>.
- Dafflon, B., Hubbard, S.S., Ulrich, C., Peterson, J.E., 2013. Electrical conductivity imaging of active layer and permafrost in an Arctic ecosystem, through advanced inversion of electromagnetic induction data. *Vadose Zone J.* 12. <http://dx.doi.org/10.2136/vzj2012.0161>.
- Doetsch, J., Linde, N., Vogt, T., Binley, A., Green, A.G., 2012. Imaging and quantifying salt-tracer transport in a riparian groundwater system by means of 3D ERT monitoring. *Geophysics* 77, B207–B218. <http://dx.doi.org/10.1190/geo2012-0046.1>.
- Doetsch, J., Fiandaca, G., Auken, E., Christiansen, A.V., Cahill, A.G., Jakobsen, R., 2015. Field-scale time-domain spectral induced polarization monitoring of geochemical changes induced by injected CO₂ in a shallow aquifer. *Geophysics* 80, WA113–WA126. <http://dx.doi.org/10.1190/geo2014-0315.1>.
- Fiandaca, G., Auken, E., Christiansen, A.V., Gazoty, A., 2012. Time-domain-induced polarization: full-decay forward modeling and 1D laterally constrained inversion of Cole–Cole parameters. *Geophysics* 77, E213–E225. <http://dx.doi.org/10.1190/geo2011-0217.1>.
- Fiandaca, G., Ramm, J., Binley, A., Gazoty, A., Christiansen, A.V., Auken, E., 2013. Resolving spectral information from time domain induced polarization data through 2-D inversion. *Geophys. J. Int.* 192, 631–646. <http://dx.doi.org/10.1093/gji/ggs060>.
- Fiandaca, G., Christiansen, A.V., Auken, E., 2015. Depth of investigation for multi-parameter inversions. *EAGE Near Surface Geoscience 2015, We21C07*, Torino, Italy.
- Flores Orozco, A., Williams, K.H., Long, P.E., Hubbard, S.S., Kemna, A., 2011. Using complex resistivity imaging to infer biogeochemical processes associated with bioremediation of an uranium-contaminated aquifer. *J. Geophys. Res.* 116, G03001. <http://dx.doi.org/10.1029/2010JG001591>.
- Gangodagamage, C., Rowland, J.C., Hubbard, S.S., Brumby, S.P., Liljedahl, A.K., Wainwright, H., Wilson, C.J., Altmann, G.L., Dafflon, B., Peterson, J., Ulrich, C., Tweedie, C.E., Wulfschleger, S.D., 2014. Extrapolating active layer thickness measurements across Arctic polygonal terrain using LiDAR and NDVI data sets. *Water Resour. Res.* 50 (8), 6339–6357. <http://dx.doi.org/10.1002/2013WR014283>.
- Hansen, B.U., Elberling, B., Humlum, O., Nielsen, N., 2006. Meteorological trends (1991–2004) at Arctic Station, Central West Greenland (69°15′N) in a 130 years

- perspective. *Geogr. Tidsskr. Dan. J. Geogr.* 106, 45–55. <http://dx.doi.org/10.1080/00167223.2006.10649544>.
- Hauck, C., 2002. Frozen ground monitoring using DC resistivity tomography. *Geophys. Res. Lett.* 29, 2016. <http://dx.doi.org/10.1029/2002GL014995>.
- Hayes, D.J., Kicklighter, D.W., McGuire, A.D., Chen, M., Zhuang, Q., Yuan, F., Melillo, J.M., Wulfschleger, S.D., 2014. The impacts of recent permafrost thaw on land-atmosphere greenhouse gas exchange. *Environ. Res. Lett.* 9, 045005. <http://dx.doi.org/10.1088/1748-9326/9/4/045005>.
- Hilbich, C., Hauck, C., Hoelzle, M., Scherler, M., Schudel, L., Völksch, I., Vonder Mühll, D., Mäusbacher, R., 2008. Monitoring mountain permafrost evolution using electrical resistivity tomography: a 7-year study of seasonal, annual, and long-term variations at Schilthorn, Swiss Alps. *J. Geophys. Res.* 113, F01S90. <http://dx.doi.org/10.1029/2007JF000799>.
- Hilbich, C., Fuss, C., Hauck, C., 2011. Automated time-lapse ERT for improved process analysis and monitoring of frozen ground. *Permafrost. Periglacial Process.* 22, 306–319. <http://dx.doi.org/10.1002/ppp.732>.
- Hoekstra, P., Sellmann, P., Delaney, A., 1975. Ground and airborne resistivity surveys of permafrost near Fairbanks, Alaska. *Geophysics* 40, 641–656. <http://dx.doi.org/10.1190/1.1440555>.
- Hollesen, J., Elberling, B., Jansson, P.E., 2011. Future active layer dynamics and carbon dioxide production from thawing permafrost layers in Northeast Greenland. *Glob. Chang. Biol.* 17, 911–926. <http://dx.doi.org/10.1111/j.1365-2486.2010.02256.x>.
- Hönig, M., Tezkan, B., 2007. 1D and 2D Cole–Cole-inversion of time-domain induced-polarization data. *Geophys. Prospect.* 55, 117–133. <http://dx.doi.org/10.1111/j.1365-2478.2006.00570.x>.
- Hubbard, S.S., Gangodagamage, C., Dafflon, B., Wainwright, H., Peterson, J., Gusmeroli, A., Ulrich, C., Wu, Y., Wilson, C., Rowland, J., Tweedie, C., Wulfschleger, S.D., 2013a. Quantifying and relating land-surface and subsurface variability in permafrost environments using LiDAR and surface geophysical datasets. *Hydrogeol. J.* 21, 149–169. <http://dx.doi.org/10.1007/s10040-012-0939-y>.
- Hubbard, C., West, L., Rodriguez-Blanco, J., Shaw, S., 2013b. Laboratory study of spectral induced polarization responses of magnetite–Fe²⁺ + redox reactions in porous media. *Geophysics* 79, D21–D30. <http://dx.doi.org/10.1190/geo2013-0079.1>.
- Ingeman-Nielsen, T., Tomašková, S., Høgsholt, S., Mulvad, S., Trabjerg, K., 2013. Comparison of alternative electrode types for improvement of electrode-ground contact in high-latitude permafrost monitoring. Presented at the 2nd International Workshop on Geoelectrical Monitoring, Vienna, Austria.
- Johnson, T.C., Versteeg, R.J., Ward, A., Day-Lewis, F.D., Revil, A., 2010. Improved hydrogeophysical characterization and monitoring through parallel modeling and inversion of time-domain resistivity and induced-polarization data. *Geophysics* 75, Wa27–Wa41. <http://dx.doi.org/10.1190/1.3475513>.
- Kemna, A., Weigand, M., Zimmermann, E., 2014. Resistivity and SIP response of rocks during freezing and thawing. Presented at the 3rd International Workshop on Induced Polarization, Ile d'Oléron, France.
- Krautblatter, M., Hauck, C., 2007. Electrical resistivity tomography monitoring of permafrost in solid rock walls. *J. Geophys. Res.* 112, F02S20. <http://dx.doi.org/10.1029/2006JF000546>.
- Krautblatter, M., Verleysdonk, S., Flores-Orozco, A., Kemna, A., 2010. Temperature-calibrated imaging of seasonal changes in permafrost rock walls by quantitative electrical resistivity tomography (Zugspitze, German/Austrian Alps). *J. Geophys. Res. Earth Surf.* 115, F02003. <http://dx.doi.org/10.1029/2008JF001209>.
- LaBrecque, D.J., Yang, X., 2001. Difference inversion of ERT data: a fast inversion method for 3-D in situ monitoring. *J. Environ. Eng. Geophys.* 6, 83–89. <http://dx.doi.org/10.4133/JEEG6.2.83>.
- Lesmes, D.P., Frye, K.M., 2001. Influence of pore fluid chemistry on the complex conductivity and induced polarization responses of Berea sandstone. *J. Geophys. Res.* 106, 4079–4090. <http://dx.doi.org/10.1029/2000JB900392>.
- Loke, M.H., Chambers, J.E., Ogilvy, R.D., 2006. Inversion of 2D spectral induced polarization imaging data. *Geophys. Prospect.* 54, 287–301. <http://dx.doi.org/10.1111/j.1365-2478.2006.00537.x>.
- Mishra, U., Riley, W.J., 2014. Active-layer thickness across Alaska: comparing observation-based estimates with CMIP5 earth system model predictions. *Soil Sci. Soc. Am. J.* 78, 894–902. <http://dx.doi.org/10.2136/sssaj2013.11.0484>.
- Oldenburg, D., Li, Y., 1994. Inversion of induced polarization data. *Geophysics* 59, 1327–1341. <http://dx.doi.org/10.1190/1.1443692>.
- Pelton, W., Ward, S., Hallof, P., Sill, W., Nelson, P., 1978. Mineral discrimination and removal of inductive coupling with multifrequency ip. *Geophysics* 43, 588–609. <http://dx.doi.org/10.1190/1.1440839>.
- Revil, A., Karoulis, M., Johnson, T., Kemna, A., 2012. Review: some low-frequency electrical methods for subsurface characterization and monitoring in hydrogeology. *Hydrogeol. J.* 20, 617–658. <http://dx.doi.org/10.1007/s10040-011-0819-x>.
- Slater, L., Lesmes, D., 2002. IP interpretation in environmental investigations. *Geophysics* 67, 77–88. <http://dx.doi.org/10.1190/1.1451353>.
- Slater, L., Choi, J., Wu, Y., 2005. Electrical properties of iron-sand columns: implications for induced polarization investigation and performance monitoring of iron-wall barriers. *Geophysics* 70, G87–G94. <http://dx.doi.org/10.1190/1.1990218>.
- Slater, L., Ntarlagiannis, D., Wishart, D., 2006. On the relationship between induced polarization and surface area in metal-sand and clay-sand mixtures. *Geophysics* 71, A1–A5. <http://dx.doi.org/10.1190/1.2187707>.
- Ulrich, C., Slater, L., 2004. Induced polarization measurements on unsaturated, unconsolidated sands. *Geophysics* 69, 762–771. <http://dx.doi.org/10.1190/1.1759462>.
- Vignoli, G., Fiandaca, G., Christiansen, A.V., Kirkegaard, C., Auken, E., 2015. Sharp spatially constrained inversion with applications to transient electromagnetic data. *Geophys. Prospect.* 63, 243–255. <http://dx.doi.org/10.1111/1365-2478.12185>.
- Wild, B., Schneckner, J., Alves, R.J.E., Barsukov, P., Bárta, J., Čapek, P., Gentsch, N., Gittel, A., Guggenberger, G., Lashchinskiy, N., Mikutta, R., Rusalimova, O., Šantrůčková, H., Shubitova, O., Urich, T., Watzka, M., Zrazhevskaya, G., Richter, A., 2014. Input of easily available organic C and N stimulates microbial decomposition of soil organic matter in Arctic permafrost soil. *Soil Biol. Biochem.* 75, 143–151. <http://dx.doi.org/10.1016/j.soilbio.2014.04.014>.
- Williams, K.H., Kemna, A., Wilkins, M.J., Druhan, J., Arntzen, E., N'Guessan, A.L., Long, P.E., Hubbard, S.S., Banfield, J.F., 2009. Geophysical monitoring of coupled microbial and geochemical processes during stimulated subsurface bioremediation. *Environ. Sci. Technol.* 43, 6717–6723. <http://dx.doi.org/10.1021/es900855j>.
- Wu, Y., Hubbard, S.S., Ulrich, C., Wulfschleger, S.D., 2013. Remote monitoring of freeze-thaw transitions in Arctic soils using the complex resistivity method. *Vadose Zone J.* 12 (1). <http://dx.doi.org/10.2136/vzj2012.0062>.
- Yoshioka, K., Zhdanov, M.S., 2005. Three-dimensional nonlinear regularized inversion of the induced polarization data based on the Cole–Cole model. *Physics of the Earth and Planetary Interiors, Electromagnetic Induction in the Earth Electromagnetic Induction in the Earth* 150, pp. 29–43. <http://dx.doi.org/10.1016/j.pepi.2004.08.034>.
- Yuval, Oldenburg, D., 1997. Computation of Cole–Cole parameters from IP data. *Geophysics* 62, 436–448. <http://dx.doi.org/10.1190/1.1444154>.